### Topological Transition in Spiral Elastic Valley Metamaterials

Shuaifeng Lio and Jinkyu Yang\*

Department of Aeronautics and Astronautics, University of Washington, Seattle, Washington, 98195-2400, USA

(Received 13 November 2020; revised 13 December 2020; accepted 4 January 2021; published 28 January 2021)

Elastic valley metamaterials offer an excellent platform to manipulate elastic waves and have potential applications in energy harvesting and elastography. Here we introduce a series of strategies to realize a topological transition in spiral elastic valley metamaterials by parameter modulations. We show the evolution of the Berry curvature and valley Chern number as a function of inherent parameters of a spiral, which further results in a general scheme to achieve topological valley edge states. Our strategy leverages multiple degrees of freedom in spiral elastic valley metamaterials to provide enhanced opportunities for desired topological states.

DOI: 10.1103/PhysRevApplied.15.014058

#### I. INTRODUCTION

Topological valley metamaterials have had a remarkable impact not only on condensed-matter physics but also on manipulation of waves in electronics, photonics, and phononics [1–9]. Wave propagation in topological valley metamaterials has prominent applications in informationcarrier and light modulation with its remarkable feature: robust valley-polarized transport [1–8,10,11]. Therein, a topological transition is a necessary process in metamaterials to realize topological states. Several strategies have been proposed to achieve the topological transition. For example, the inherent degree of freedom, such as adjusting the geometric parameters, can be exploited to invert the topological phase of metamaterials [4,6,9,12]. Besides, the external degree of freedom, such as deformation, can also affect the band inversion dynamically [13,14]. However, existing metamaterials still lack of the control knob to generate the desired topological phase at will. One of the reasons is that the inherent simple structures are insufficient to manipulate the geometric parameters.

Recently, spiral and chiral elements have been used for the construction of metamaterials, realizing remarkable achievements [9,15–19]. Especially, an elastic valley metamaterial that consists of a hard spiral in a soft hexagonal matrix was proposed as a design to achieve valley topological insulators [9]. In contrast to conventional valley systems, spiral elastic valley metamaterials have high complexity of internal structure, which has a series of design parameters to manipulate. For example, this spiral system possesses an inherent chiral anisotropy, which results in valley anisotropy and the exceptional Berry curvature distribution. On this basis, the elastic topological valley edge

state relying on frequency has been demonstrated to have potential applications in signal processing and frequency selection.

Although this spiral system has shown promising properties and greater controllability in comparison with the symmetric valley system, there remain several natural questions about this valley system. For example, since this is a chiral anisotropic system, how does the chirality affect the topological properties? How does the topological transition happen in an asymmetric system? Addressing these challenging questions is important to understand and enrich the intrinsic physics of topological valley states.

In this article, we report a topological transition via parameter modulations in spiral elastic metamaterials. We discuss the effect of chirality, rotation angle, number of turns, and thickness of the spiral on the topological properties in terms of the Berry curvature and valley Chern number. Topological transition of spiral elastic metamaterials is clearly shown by the inversion of the Berry curvature and valley Chern number. After the key factors contributing to the topological transition are determined, we propose a general scheme to generate the desired topological phase of these elastic metamaterials. Furthermore, we demonstrate topological valley edge states by using this general scheme. Thereby, our strategy provides enhanced degrees of freedom and opportunities to achieve a topological transition by leveraging the spiral architecture's parameter modulations.

### II. TOPOLOGICAL TRANSITION VIA PARAMETER MODULATIONS

Figure 1 shows a schematic of the spiral elastic valley metamaterial considered in this study. A hard spiral made of polylactic acid (PLA) is embedded as a scatterer in a triangular unit-cell matrix made of soft hydrogel.

<sup>\*</sup>jkyang@aa.washington.edu

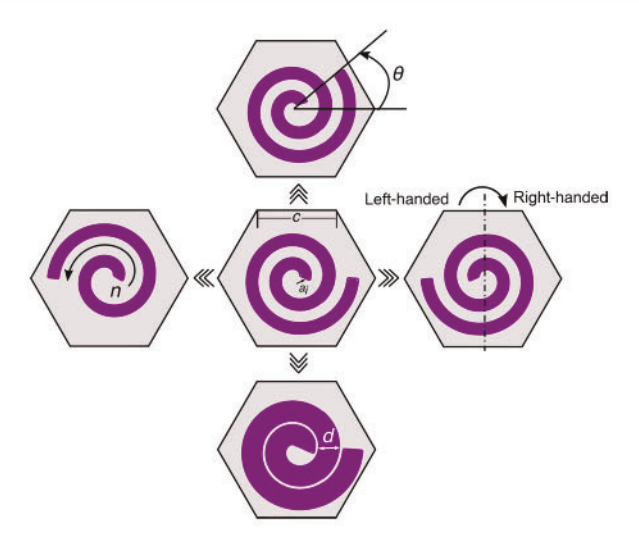


FIG. 1. Schematics of spiral elastic valley metamaterials. The scatterer (Archimedean-spiral structure) is shown in purple and the soft matrix is shown in beige. Modulations of chirality, rotation angle, number of turns, and thickness of the scatterer are illustrated on the right, at the top, on the left, and at the bottom, respectively.

The mechanical properties of the spiral PLA are as follows: mass density  $1250 \text{ kg/m}^3$ , Young's modulus 2.1 GPa, and Poisson's ratio 0.36. The mechanical properties of the soft hydrogel are as follows: mass density  $1000 \text{ kg/m}^3$ , Young's modulus 18 kPa, and Poisson's ratio 0.5. Four parameter modulations are shown around the original unit cell of the spiral elastic metamaterial, where the side of the hexagon c=14 mm and the initial spiral radius  $a_i=1.5$  mm. Modulations of chirality C, rotation angle  $\theta$ , number of turn n, and thickness of the spiral d are illustrated counterclockwise. For simplicity, we denote our spiral elastic metamaterial by  $(C, \theta \text{ (deg)}, n, d \text{ (mm)})$  to discuss the topological transition. All simulations are done under the plane-strain condition with use of COMSOL Multiphysics.

First, we investigate the effect of the rotation angle of the spiral around the center of the hexagon  $(\theta)$  on the topological properties. According to our previous work, there exists a band inversion under certain circumstances between the second band and the third band [9]. Therefore, we focus on these two bands of (right-handed,  $\theta$ , 2, 2). We calculate two bands around the K point when the spiral is rotated around the center from  $20^{\circ}$  to  $40^{\circ}$  with an increment of  $1^{\circ}$ . The blue line in Fig. 2(a) represents the maximum frequency of the second band and the red line represents the minimum frequency of the third band. The enclosed area, which is the band-gap range, experiences an open-close-reopen process (see the narrowing band gap around the  $30^{\circ}$  region). Because of the low-order symmetry of the spiral, the band gap cannot completely close.

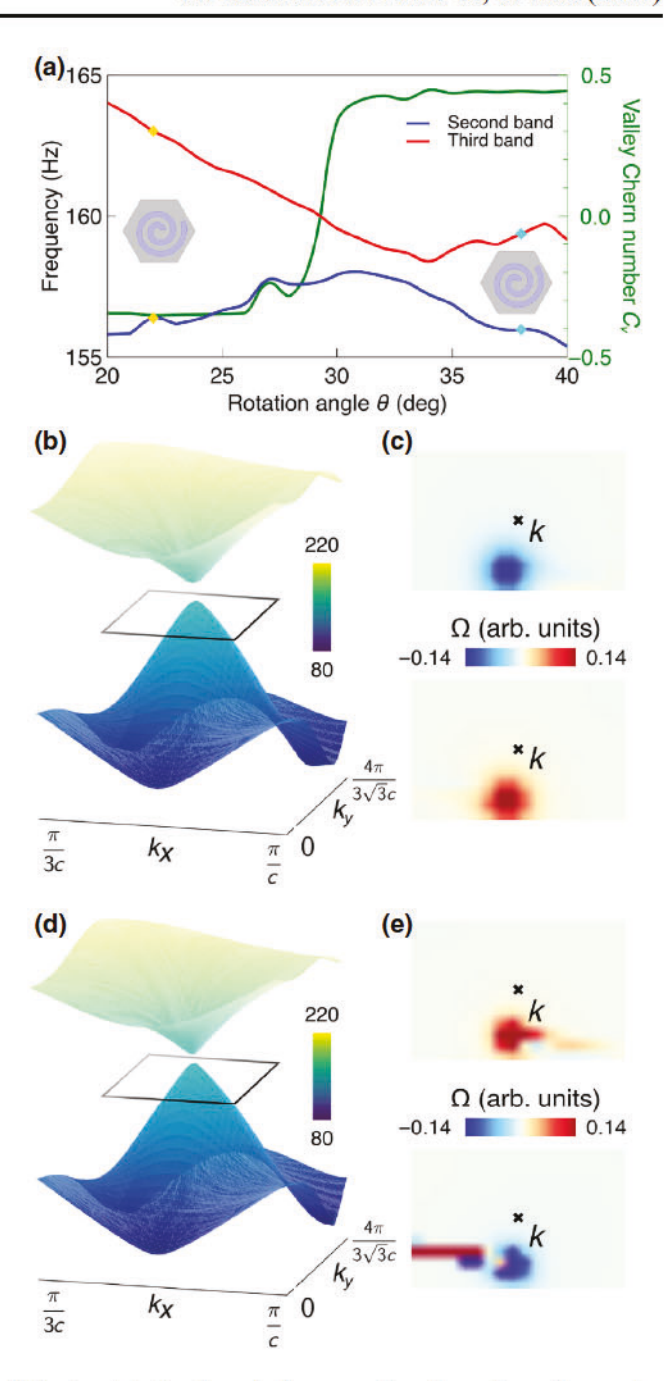


FIG. 2. (a) Band evolution as a function of rotation angle. The blue and red lines represent the maximum frequency of the second band and the minimum frequency of the third band, respectively, as the spiral rotates. The green line indicates the valley Chern number as a function of rotation angle. (b) Band structure of (right-handed,  $22^{\circ}$ , 2, 2) elastic metamaterial, which is marked by yellow diamonds in (a). (c) The corresponding Berry curvature. Black crosses indicate the corners of the Brillouin zone (K point). (d) Band structure of (right-handed,  $38^{\circ}$ , 2, 2) elastic metamaterial, which is marked by cyan diamonds in (a). (e) The corresponding Berry curvature. Black crosses indicate the corners of the Brillouin zone (K point). The area for the calculation of the Berry curvature is shown in (b),(d) in black lines, which spans  $k_x$  from  $8\pi/15c$  to  $4\pi/5c$  and  $k_y$  from  $\pi/(2\sqrt{3}c)$  to  $5\pi/(6\sqrt{3}c)$ .

We calculate the valley Chern number  $C_v = (1/2\pi) \int i\nabla_k \times u(\mathbf{k}) |\nabla_k| u(\mathbf{k}) d^2\mathbf{k}$  based on the third band using the numerical method [20]. As shown in Fig. 2(a), the green line indicates that the valley Chern number has a sudden increase at around 29°, suggesting that our spiral elastic metamaterial has a topological transition (see Appendix A for the explanation of this transition at 29° by introduction of the pseudospin angular momentum). Within one topological phase, the valley Chern number has little fluctuation, which suggests that the rotation has little effect on the valley Chern number until it crosses the critical angle around 29°. Besides, the valley Chern number is always within (-0.5, 0.5) due to the strong spatial inversion symmetry breaking [9,21–23].

Figure 2(b) shows the band structure around the K point of (right-handed, 22°, 2, 2) as indicated by the yellow diamonds in Fig. 2(a). The second band and the third band behave like the typical valley structure with a small band gap. The Berry-curvature distributions of the corresponding bands calculated within the black lines [Fig. 2(b)] are shown in Fig. 2(c), where they have the opposite sign and the extrema of the Berry curvature deviate from the K point. This discrepancy is caused by the mismatch between the asymmetric spiral and the triangular lattice [9]. When the spiral continues rotating to 38° until it has the configuration (right-handed, 38°, 2, 2) [cyan diamonds in Fig. 2(c)], the band structure illustrated in Fig. 2(d) is similar to that of the structure with the configuration (right-handed, 22°, 2, 2). However, the Berry-curvature

distributions are completely distinct. The Berry curvature of the second band has negative values and that of the third band has positive values. This inversion of the Berry curvature indicates the band inversion and the topological transition. The band inversion often reflects the eigenmodes of metamaterials, but the eigenmodes of these two configurations at the *K* point do not show the swap of the two bands clearly. Instead, the band inversion reflects the pseudospin of the phonon in the unit cell, which indicates different valley polarization (see Appendix A). This is one of the unique aspects of our spiral valley system in contrast to the conventional symmetric valley system.

A spiral is a natural chiral element, where right-handed and left-handed spirals can be transformed by parity inversion [24,25]. To explore the effect of chirality on the topology of the bands, we fix d=2 mm and choose several configurations made from combinations among chirality, rotation angle, and number of turns. Likewise, we calculate the Berry curvature around the K point and integrate it for the valley Chern number for all configurations. The valley Chern number calculated here is based on the third band because the second band is largely coupled with the first band, which will result in inaccuracy of the valley Chern number.

In Fig. 3(a), green filled circles show the variation of the valley Chern number for (right-handed,  $\theta$ , 1.5, 2) as a function of the rotation angle, and green unfilled circles represent the variation of the valley Chern number for (left-handed,  $\theta$ , 1.5, 2). Likewise, in Fig. 3(b),

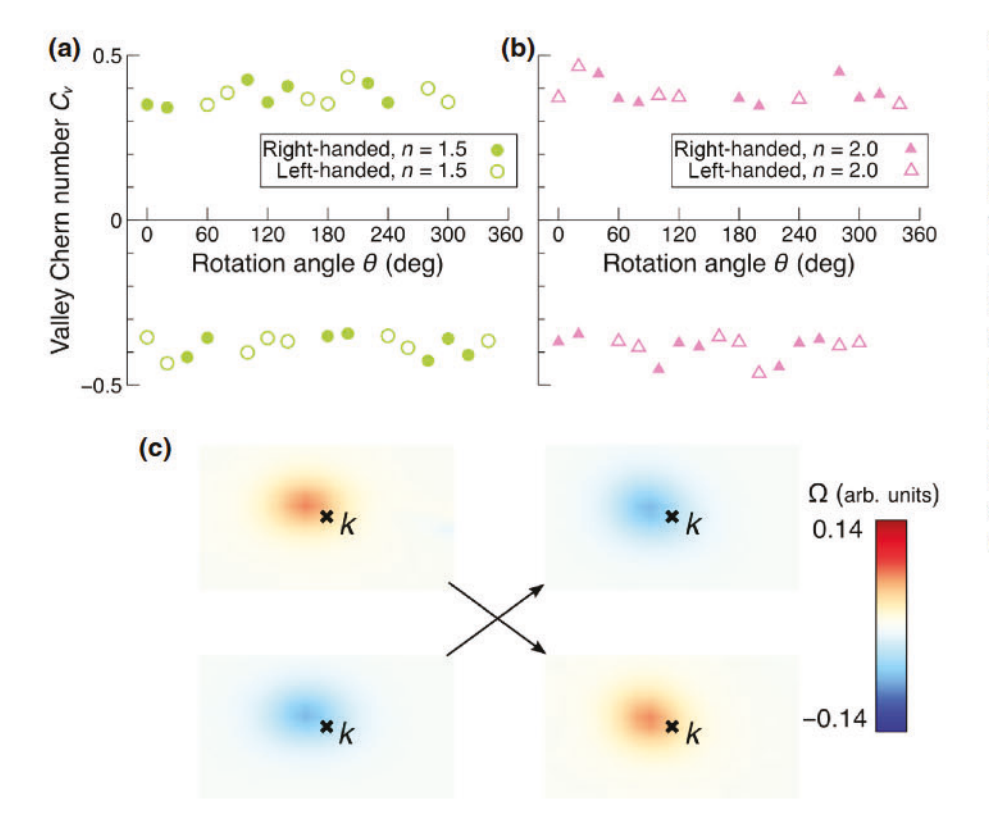


FIG. 3. (a),(b) Evolution of the valley Chern number for elastic metamaterials for different chiralities. (a) Valley Chern numbers for (right-handed,  $\theta$ , 1.5, 2) and (left-handed,  $\theta$ , 1.5, 2) for rotation angle  $\theta$  varying from  $0^{\circ}$  to  $360^{\circ}$ shown as green filled circles and green unfilled circles, respectively. (b) Valley Chern numbers for (right-handed,  $\theta$ , 2, 2) and (left-handed,  $\theta$ , 2, 2) shown as magenta filled triangles and magenta unfilled triangles, respectively. (c) The left panel shows the Berry curvature of the third band and the second band of (left-handed, 60°, 1.5, 2) metamaterial, while the right panel shows the Berry curvature of (right-handed, 60°, 1.5, 2) metamaterial.

magenta filled triangles and unfilled triangles show the variation of the valley Chern number for (right-handed,  $\theta$ , 2, 2) and (left-handed,  $\theta$ , 2, 2), respectively. From the two graphs, the rotation is able to cause the topological transition, which confirms the conclusion in Fig. 2. More notably, massive calculations of valley Chern numbers of different configurations shows that when the chirality of the spiral changes (e.g., from a right-handed to lefthanded spiral), the sign of the valley Chern number always changes, suggesting that the topological transition should happen when the chirality changes. That is, we find that the Chern-number data points of the left-handed counterparts (unfilled circles or triangles) can always be found on the other side of the right-handed geometries (filled circles or triangles). Note that we calculate the valley Chern number from 0° to 360° with an increment 20° but several missing data points are found because Berry curvatures of some configurations are distributed with both positive and negative values, which poses a challenge to the integral. We also observe in passing that when the number of turns n changes from 1.5 to 2, the sign of the valley Chern number is flipped, which was shown in previous work [9].

We then take (left-handed,  $60^{\circ}$ , 1.5, 2) and (right-handed,  $60^{\circ}$ , 1.5, 2) as examples to demonstrate the topological transition caused by the chirality modulation. The top row in Fig. 3(c) shows Berry-curvature distributions for the third bands in both cases, while the bottom row shows Berry-curvature distributions of the second bands. The Berry-curvature distribution, likewise, deviates from the K point because of the mismatch between the asymmetric spiral and the triangular lattice. When the

left-handed spiral is transformed to the right-handed spiral, there is a clear sign flip of the Berry curvature, suggesting that the topological transition happens in this process.

To continue discussing the effect of the thickness of the spiral on the topological properties, we calculate the valley Chern number for several elastic metamaterials with different configurations (C,  $60^{\circ}$ , n, d). In Fig. 4, for variation of d from 1 to 4 mm, the evolution of the valley Chern number of (right-handed,  $60^{\circ}$ , 1.5, d) is shown as a solid red line. The corresponding Berry-curvature distribution is shown near the solid red line. We notice that apart from the deviation of the Berry curvature, the magnitude of the Berry curvature becomes smaller and the distribution becomes dispersed when d increases to 4 mm, resulting in a decreasing valley Chern number. Since the spiral approaches a solid circle with the increase of d, this will reduce the broken spatial inversion, which will result in a decrease of the Berry curvature.

As discussed in the previous section, a change of chirality can induce the topological transition. The dashed red line represents the evolution of the valley Chern number of (left-handed,  $60^{\circ}$ , 1.5, d), which displays positive values. The corresponding Berry curvatures are shown beside the dashed red line. They have the same trend as in the previous case. Similarly, we can deduce that the valley Chern number of (right-handed,  $60^{\circ}$ , 2, d), as shown by the solid blue line, will be opposite that of (right-handed,  $60^{\circ}$ , 1.5, d), which has negative values. We also notice that increasing n from 1.5 to 2 will increase the absolute value of valley Chern number for  $\theta = 60^{\circ}$  when the chirality is the same. However, for other rotation angles, the change of the absolute value of the valley Chern number may be

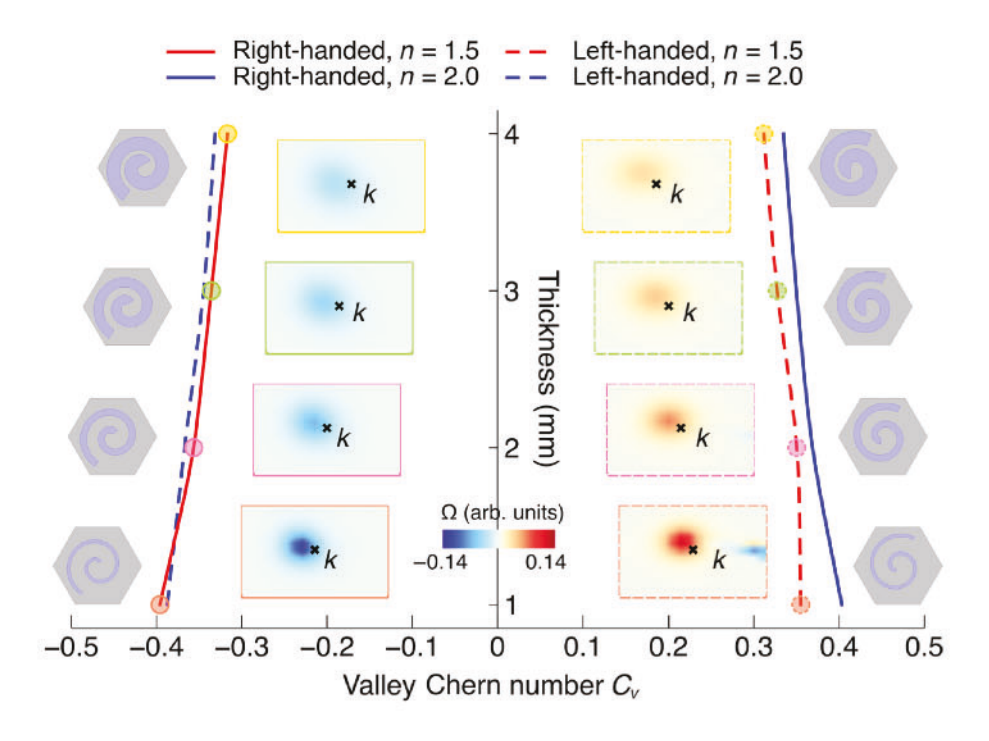


FIG. 4. Evolution of valley Chern number for elastic metamaterials for different thicknesses. Valley Chern numbers for (right-handed, 60°, 1.5, *d*), (left-handed, 60°, 1.5, *d*), (right-handed, 60°, 2, *d*) metamaterials for thickness *d* varying from 1 to 4 mm, shown as the solid red line, the dashed red line, the solid blue line, and the dashed blue line, respectively. The corresponding Berry curvatures of the third band are shown beside the lines. The corresponding configurations are also shown beside the lines.

different when n varies from 1.5 to 2 (see Appendix B and Fig. 7).

According to the above analysis, we can conclude that chirality C, rotation angle  $\theta$ , and the number of turns n of the spiral play an important role in the topological transition. Chirality transformation causes a topological transition when the parity changes. Rotation will also change the topology of bands and is related to the symmetry of the lattice. When the rotation angle varies from 0° to 360°, there is a periodic change of topological properties, where six topological transition points exist in this process determined by the triangular lattice. We also confirm that changing number of turns results in a topological transition. However, changing the thickness of the spiral only changes the valley Chern number instead of flipping the sign. In possession of information on the topological transition via parameter modulation, we can design the desired topological phase of spiral elastic valley metamaterials.

### III. ELASTIC TOPOLOGICAL VALLEY EDGE STATES

After obtaining the general scheme for generating different topological phases, we create an elastic topological insulator on the basis of our conclusion in the previous section. We can confirm that (right-handed, 60°, 1.5, 2) has a positive Berry curvature and a negative Berry curvature in its second and third bands, respectively, as observed from Fig. 3(b). To find an elastic metamaterial with the opposite topological properties and fully reflect our previous conclusion, we choose a left-handed spiral first, which will invert the topological phase once [i.e., (right-handed,  $60^{\circ}$ , 1.5, 2)  $\rightarrow$  (left-handed,  $60^{\circ}$ , 1.5, 2)]. Then we are aware that rotation also induces a topological transition, so  $\theta = 0^{\circ}$  is chosen to invert the topological phase twice [i.e., (left-handed,  $60^{\circ}$ , 1.5, 2)  $\rightarrow$  (left-handed,  $0^{\circ}$ , 1.5, 2)]. After we select n=2 as the number of turns of the spiral, we invert the topological phase three times in total [i.e., (left-handed,  $0^{\circ}$ , 1.5, 2)  $\rightarrow$  (left-handed,  $0^{\circ}$ , 2, 2)]. Thus, we have the opposite topological phase if we choose (lefthanded, 0°, 2, 2) compared with the original (right-handed, 60°, 1.5, 2). Lastly, to ensure that we have an overlapping band gap between two components, we change the thickness d (see Appendix C, which shows the frequency range of the band gap as a function of d). Conclusively, (lefthanded, 0°, 2, 1) is chosen to have a topological phase opposite that of and a band gap overlapping with that of (right-handed, 60°, 1.5, 2). Therefore, we denote the generated elastic valley metamaterial as (right-handed, 60°, 1.5, 2 | left-handed, 0°, 2, 1).

Figure 5(a) illustrates the projected band structure calculated for a sandwiched supercell (right-handed,  $60^{\circ}$ , 1.5, 2 | left-handed,  $0^{\circ}$ , 2, 1 | right-handed,  $60^{\circ}$ , 1.5, 2). The geometry of the supercell is shown in Fig. 5(b), where the interface is a zigzag. In the band structure, the bulk

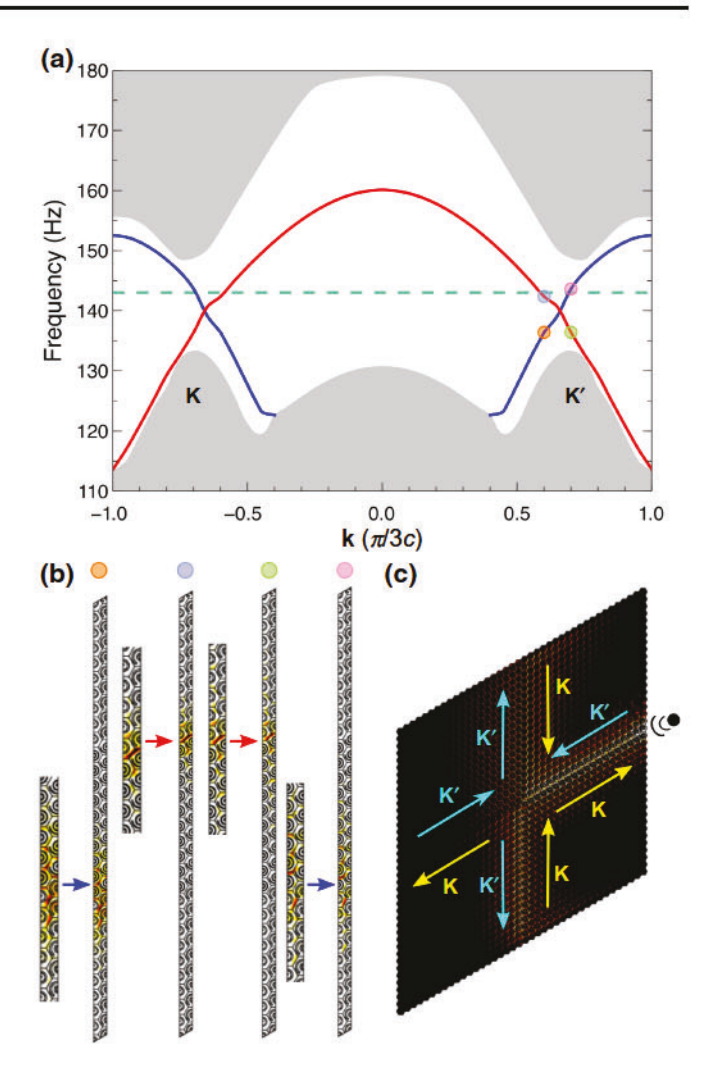


FIG. 5. (a) The projected band structure of the (right-handed,  $60^{\circ}$ , 1.5,  $2 \mid$  left-handed,  $0^{\circ}$ , 2, 1) metamaterial. Topological interface states are shown as red and blue lines. Bulk modes are shown in gray. Four markers are placed at k = 0.6 and k = 0.7, respectively. (b) The displacement fields corresponding to markers in (a). The arrows indicate the position of the interface. Enlarged displacement fields near the interfaces are shown beside the arrows. (c) Propagation of elastic waves along the interface. The directions of topological edge states projected by different valleys are marked by the yellow and cyan arrows. At a frequency of 143 Hz, which is shown by dashed green line in (a), elastic waves propagate along the interface and through the bend.

states are shown in gray. Because the two elastic metamaterials are topologically different, two topological interface states appear within the band gap as a result of the bulkedge correspondence, as displayed by red and blue lines. We choose four points on the topological interface states located at  $\mathbf{k} = 0.6$  and  $\mathbf{k} = 0.7$ . By our checking the eigendisplacement-field at these points, Fig. 5(b) indicates the vibrations are concentrated around the interface marked by the arrows (magnified views of the interfaces are shown in the insets). As shown by the leftmost (orange) and

rightmost (pink) cases in Fig. 5(b), the eigen-displacement-fields corresponding to the blue line in Fig. 5(a) show the topological edge states located at the interface between (right-handed,  $60^{\circ}$ , 1.5, 2) and (left-handed,  $0^{\circ}$ , 2, 1) (see the blue arrows). On the other hand, the eigen-displacement-fields for the red line in Fig. 5(a) represent the topological edge states located at the interface between (left-handed,  $0^{\circ}$ , 2, 1) and (right-handed,  $60^{\circ}$ , 1.5, 2) [see the red arrows in the blue and green cases in Fig. 5(b)].

We note again that the supercell in Fig. 5 is composed of the two types of spiral architectures that underwent topological flipping between them three times (i.e., chirality, rotation angle, and number of turn changes). In Appendix D, we present the projected band structures of the supercells with (i) one-time topological flipping by chirality-only change [i.e., (right-handed, 60°, 1.5, 2) and (left-handed, 60°, 1.5, 2)] and (ii) two-time topological flipping by chirality and rotation-angle change [i.e., (righthanded, 60°, 1.5, 2) and (left-handed, 0°, 1.5, 2)]. We confirm that as predicted and guided by our parametric studies in Sec. II, one-time (two-time) flipping results in a domain boundary with a distinctive (identical) topological nature. We demonstrate that this, in turn, causes the appearance (disappearance) of the topological interface states (see Appendix D for details).

Returning to the configuration in Fig. 5, we now explore the topologically protected transport of elastic waves in this elastic metamaterial. We construct a two-part metamaterial consisting of (right-handed, 60°, 1.5, 2) at the bottom left and top right and (left-handed, 0°, 2, 1) at the bottom right and top left, as shown in Fig. 5(c). One of the most-important features of the edge states in topological valley metamaterials lies in the valley-polarized nature. In our case, when a vibration source with a frequency of 143 Hz [marked in the dashed green line in Fig. 5(a)] is set on the right side of our elastic metamaterial, the topological valley edge states between (left-handed, 0°, 2, 1) and (right-handed, 60°, 1.5, 2) are excited. As shown in Fig. 5(c), the elastic wave travels along the path at the beginning, and when it arrives at the intersection, it propagates both upwards and downwards, but it does not propagate forwards. This indicates that the mode generated at the beginning can couple with the upward mode and the downward mode. We notice that there is a sharp corner in the upward direction and an obtuse corner in the downward direction, which demonstrates the reflection immunity of topological valley edge states to path bending. The cross-waveguide splitter also demonstrates the valley-polarized elastic wave propagation [26–30]. The generated forward elastic wave is projected by the K' valley according to the group velocity shown in the projected band structure [Fig. 5(a)]. The propagation direction of K-valley-projected (K'-valley projected) elastic waves is marked in Fig. 5(c) by yellow (cyan) arrows. Therefore, the elastic wave will travel along the cyan arrows, which

forms an elastic wave splitter resulting from its valley polarization.

#### IV. CONCLUSIONS

In this study, we investigate topological properties of a spiral structure with multiple degrees of freedom in detail. We demonstrate computationally that the inherent geometrical parameters of the spiral architecture, such as chirality, rotation angle, and number of turns, can induce evolution of the Berry curvature and valley Chern number of a spiral elastic valley metamaterial, thereby resulting in a landscape change of the topological characteristics. Knowledge of different roles played by spiral parameters enhances our understanding of the elastic topological phase transition using parameter modulation in our system and opens avenues for topological state manipulation. This strategy based on an asymmetric spiral architecture gives us the possibility to realize and control a topological interface state in a more-controllable and more-efficient manner compared with symmetric valley architectures. Our research may not be limited only to the monofilar spiral, but can be extended and generalized to the bifilar spiral, trifilar spiral, and so on [19,31], which may have more degrees of freedom to tune the topological properties of elastic metamaterials.

#### ACKNOWLEDGMENTS

We are grateful for the support from NSF (CAREER155 3202 and EFRI-1741685).

# APPENDIX A: BAND EVOLUTION AT THE K POINT, EIGENMODES, AND PSEUDOSPIN ANGULAR MOMENTUM

Because of the asymmetric spiral in the metamaterials, when the spiral rotates around the center, there is no degenerate point appearing at the K point, although the topological phase is indeed inverted according to Fig. 2. Figure 6(a) presents the evolution of two bands at the Kpoint as the spiral rotates around the center. It appears the periodic change of frequency does not have a degenerate point at the K point in this process as we predict. In addition, we calculate the total pseudospin angular momentum of a phonon within the unit cell using  $S = (\rho \omega/2) \mathbf{u} |\hat{\mathbf{S}}| \mathbf{u}$ , where  $\rho$  is the mass density,  $\omega$  is the angular frequency, **u** is the eigen-displacement-field, and  $\hat{S}$  is the spin-1 operator [9,32]. The dashed lines show the periodic change across the positive and negative values with a period of 60°. When the total pseudospin angular momentum is zero in the unit cell, the pseudospin nature vanishes in our elastic valley metamaterials, corresponding to the topological transition points, such as the first topological transition point at around 29°.

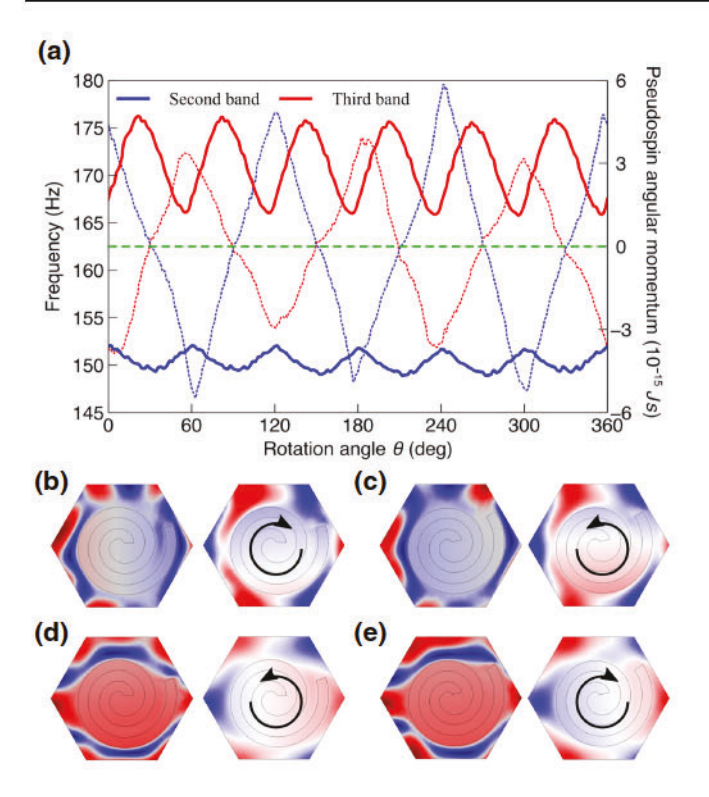


FIG. 6. (a) Evolution of the second band at the *K* point as a function of rotation angle (blue line) and the evolution of the third band at the *K* point as a function of rotation angle (red line). The corresponding dotted lines show the pseudospin angular momentum in the unit cell as a function of the rotation angle. The dashed green line represents zero pseudospin angular momentum. (b),(c) Eigen-displacement-fields and pseudospin-angular-momentum-density distribution of the third bands of (right-handed, 22°, 2, 2) and (right-handed, 38°, 2, 2), respectively. (d),(e) Eigen-displacement-fields and pseudospin-angular-momentum-density distribution of the second bands of (right-handed, 22°, 2, 2) and (right-handed, 38°, 2, 2). The curved arrows indicate pseudospin up and pseudospin down.

As mentioned in the main text, the eigenmodes at the K point do not show the inversion of the band. The eigenmodes of the third and second bands of (right-handed, 22°,

2, 2) are shown in the left panels in Figs. 6(b) and 6(d). For comparison, the eigenmodes of the third and the second bands of (right-handed, 38°, 2, 2) are shown in the left panels in Figs. 6(c) and 6(e). From the eigenmode, we cannot see any indication of band inversion or topological transition. However, the right panels in Figs. 6(b)-6(e) display the pseudospin-angular-momentum density distribution corresponding to each state. We find negative and positive total pseudospin angular momentum in the third band and the second band of (right-handed, 22°, 2, 2), representing the pseudospin-down and pseudospin-up states. In stark contrast, corresponding states of (right-handed, 38°, 2, 2) show positive and negative total pseudospin angular momentum, representing the pseudospin-up and pseudospin-down states. The inversion of pseudospin states clearly shows the topological transition. Besides, from the Berry curvature in Figs. 2(c) and 2(e), these two configurations are topologically different, which further verifies that the band inversion reflects the pseudospin of the phonon.

## APPENDIX B: VALLEY CHERN NUMBER AFFECTED BY THE NUMBER OF TURNS

The valley Chern numbers of (right-handed, 60°, 1.5, d) and (right-handed, 60°, 1.5, d) are illustrated in Fig. 4. Here we investigate the absolute values of valley Chern numbers for different rotation angles when the number of turns is changed from 1.5 to 2.0. We take (right-handed,  $\theta$ , n, 2) and (left-handed,  $\theta$ , n, 2) as examples. According to the left panel in Fig. 7, most of the green unfilled circles are above the green filled circles, suggesting that increasing the number of turns from 1.5 to 2.0 can increase the absolute value of the valley Chern number. However, there are a few cases, such as  $\theta = 120^{\circ}$  and  $\theta = 320^{\circ}$ , where the absolute value of the valley Chern number decreases when the number of turns is changed from 1.5 to 2.0. Similarly, the right panel in Fig. 7 shows that for most of the cases, increasing the number of turns from 1.5 to 2.0 can increase the absolute value of the valley Chern number.

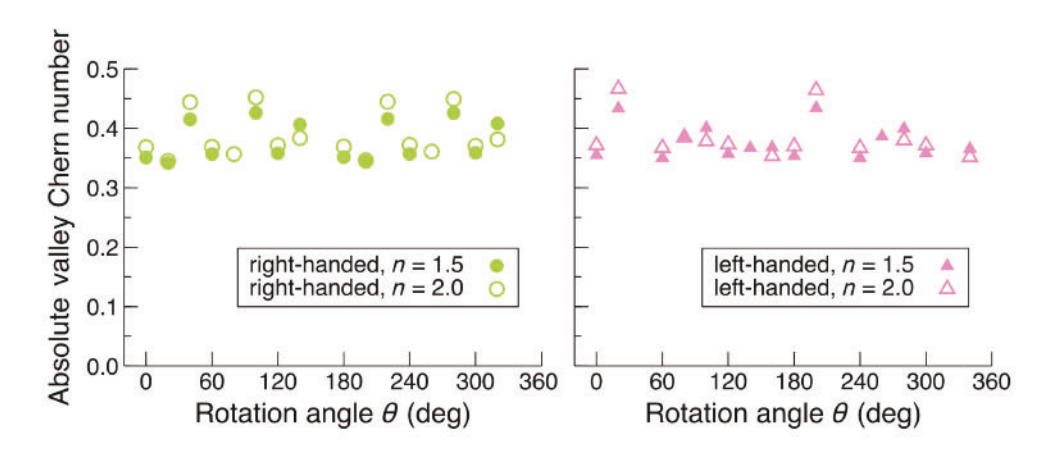


FIG. 7. Absolute values of valley Chern numbers for (right-handed,  $\theta$ , 1.5, 2) and (right-handed,  $\theta$ , 2, 2) shown as green filled circles and green unfilled circles, respectively (left panel), and absolute values of valley Chern numbers for (left-handed,  $\theta$ , 1.5, 2) and (left-handed,  $\theta$ , 2, 2) shown as magenta filled triangles and magenta unfilled triangles, respectively (right panel).

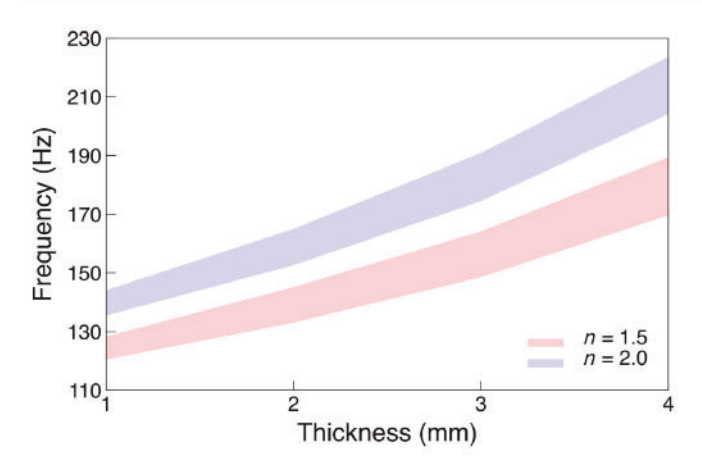


FIG. 8. Variation of band-gap range as a function thickness d for (left-handed,  $0^{\circ}$ , 1.5, d) and (left-handed,  $0^{\circ}$ , 2, d).

# APPENDIX C: BAND-GAP EVOLUTION AS A FUNCTION OF THICKNESS

After we find our desired topological phase of the spiral elastic metamaterials via modulation of chirality, rotation angle, and the number of turns, we need to find the overlapping band gap between the two metamaterials. By tuning the thickness d, we are able to adjust the band-gap range. As shown in Fig. 8, red and purple areas show the variations of band-gap ranges of (left-handed,  $0^{\circ}$ , 1.5, d) and (left-handed,  $0^{\circ}$ , 2, d), respectively. Both show a clear trend that with increase of the thickness of the spiral, the frequency increases and the band gap slightly increases. In this way, we can ensure that the two metamaterials we choose have an overlapping band gap.

# APPENDIX D: PROJECTED-BAND-STRUCTURE EVOLUTION VIA PARAMETER MODULATION

To demonstrate the topological transition via parameter modulations, we change one parameter at a time. As mentioned in the main text, we choose (right-handed, 60°, 1.5, 2) as one part of the topological insulator. For the other part, we first change the chirality from right-handed to left-handed. The left panel in Fig. 9 shows the projected band calculated for a supercell (right-handed, 60°, 1.5, 2 | left-handed, 60°, 1.5, 2 | right-handed, 60°, 1.5, 2). There are two topological interface states within the band gap, shown in red and blue, which are located at two interfaces respectively. Next we continue to change the rotation angle to 0°. This operation, along with the previous chirality change, causse two-time flipping of the topological nature, thereby returning the topological phase to the original phase. The corresponding projected band structure is shown in the right panel in Fig. 9. As predicted by our general scheme, (right-handed, 60°, 1.5, 2) and (left-handed, 0°, 1.5, 2) share the same topological

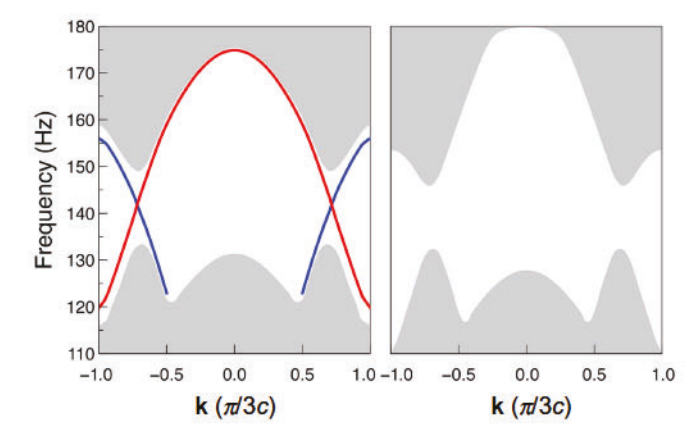


FIG. 9. Projected band structures calculated for the supercell (right-handed, 0°, 2, 1 | left-handed, 0°, 2, 1 | right-handed, 0°, 2, 1 | left-handed, 60°, 2, 1 | left-handed, 60°, 2, 1 | left-handed, 0°, 2, 1 | right-handed, 60°, 2, 1) (right panel).

phase, resulting in the complete stop band within the bulk band.

- A. Rycerz, J. Tworzydło, and C. W. J. Beenakker, Valley filter and valley valve in graphene, Nat. Phys. 3, 172 (2007).
- [2] D. Xiao, W. Yao, and Q. Niu, Valley-Contrasting Physics in Graphene: Magnetic Moment and Topological Transport, Phys. Rev. Lett. 99, 236809 (2007).
- [3] K. F. Mak, K. L. McGill, J. Park, and P. L. McEuen, The valley hall effect in MoS<sub>2</sub> transistors, Science 344, 1489 (2014).
- [4] J. W. Dong, X. D. Chen, H. Zhu, Y. Wang, and X. Zhang, Valley photonic crystals for control of spin and topology, Nat. Mater. 16, 298 (2017).
- [5] X. D. Chen, W. M. Deng, J. C. Lu, and J. W. Dong, Valley-Controlled propagation of pseudospin states in bulk metacrystal waveguides, Phys. Rev. B 97, 184201 (2018).
- [6] J. Lu, C. Qiu, M. Ke, and Z. Liu, Valley Vortex States in Sonic Crystals, Phys. Rev. Lett. 116, 093901 (2016).
- [7] R. K. Pal and M. Ruzzene, Edge waves in plates with resonators: An elastic analogue of the quantum valley hall effect, New J. Phys. 19, 025001 (2017).
- [8] J. Vila, R. K. Pal, and M. Ruzzene, Observation of topological valley modes in an elastic hexagonal lattice, Phys. Rev. B 96, 134307 (2017).
- [9] S. Li, I. Kim, S. Iwamoto, J. Zang, and J. Yang, Valley anisotropy in elastic metamaterials, Phys. Rev. B 100, 195102 (2019).
- [10] X. Xu, W. Yao, D. Xiao, and T. F. Heinz, Spin and pseudospins in layered transition metal dichalcogenides, Nat. Phys. 10, 343 (2014).
- [11] M. Yan, J. Lu, F. Li, W. Deng, X. Huang, J. Ma, and Z. Liu, On-Chip valley topological materials for elastic wave manipulation, Nat. Mater. 17, 993 (2018).

- [12] L. H. Wu and X. Hu, Scheme for Achieving a Topological Photonic Crystal by Using Dielectric Material, Phys. Rev. Lett. 114, 223901 (2015).
- [13] S. Li, D. Zhao, H. Niu, X. Zhu, and J. Zang, Observation of elastic topological states in soft materials, Nat. Commun. 9, 1370 (2018).
- [14] T. W. Liu and F. Semperlotti, Tunable Acoustic Valley-Hall Edge States in Reconfigurable Phononic Elastic Waveguides, Phys. Rev. Appl. 9, 014001 (2018).
- [15] Y. Fu, J. Li, Y. Xie, C. Shen, Y. Xu, H. Chen, and S. A. Cummer, Compact acoustic retroreflector based on a mirrored luneburg lens, Phys. Rev. Mater. 2, 105202 (2018).
- [16] T. Frenzel, M. Kadic, and M. Wegener, Three-Dimensional mechanical metamaterials with a twist, Science 358, 1072 (2017).
- [17] R. Zhu, X. N. Liu, G. K. Hu, C. T. Sun, and G. L. Huang, Negative refraction of elastic waves at the deepsubwavelength scale in a single-phase metamaterial, Nat. Commun. 5, 5510 (2014).
- [18] H. Tang, Z. Chen, N. Tang, S. Li, Y. Shen, Y. Peng, X. Zhu, and J. Zang, Hollow-Out patterning ultrathin acoustic metasurfaces for multifunctionalities using soft fiber/rigid bead networks, Adv. Funct. Mater. 28, 1801127 (2018).
- [19] A. Foehr, O. R. Bilal, S. D. Huber, and C. Daraio, Spiral-Based Phononic Plates: From Wave Beaming to Topological Insulators, Phys. Rev. Lett. 120, 205501 (2018).
- [20] T. Fukui, Y. Hatsugai, and H. Suzuki, Chern numbers in discretized brillouin zone: Efficient method of computing (spin) hall conductances, J. Phys. Soc. Japan 74, 1674 (2005).
- [21] H. Zhu, T. W. Liu, and F. Semperlotti, Design and experimental observation of valley-hall edge states in diatomic-graphene-like elastic waveguides, Phys. Rev. B 97, 174301 (2018).
- [22] I. Kim, Y. Arakawa, and S. Iwamoto, Design of GaAsbased valley phononic crystals with multiple complete

- phononic bandgaps at ultra-high frequency, Appl. Phys. Express 12, 047001 (2019).
- [23] K. Qian, D. J. Apigo, C. Prodan, Y. Barlas, and E. Prodan, Topology of the valley-chern effect, Phys. Rev. B 98, 155138 (2018).
- [24] H. Niu, S. Li, and J. Zang, Reliable and tunable elastic interface states in soft metamaterials, Phys. Status Solidi 14, 2000338 (2020).
- [25] M. Petitjean, Chirality in metric spaces, Optim. Lett. 14, 329 (2020).
- [26] X. Han, Y. G. Peng, L. Li, Y. Hu, C. Mei, D. G. Zhao, X. F. Zhu, and X. Wang, Experimental Demonstration of Acoustic Valley Hall Topological Insulators with the Robust Selection of C<sub>3V</sub>-Symmetric Scatterers, Phys. Rev. Appl. 12, 14046 (2019).
- [27] X. Cheng, C. Jouvaud, X. Ni, S. H. Mousavi, A. Z. Genack, and A. B. Khanikaev, Robust reconfigurable electromagnetic pathways within a photonic topological insulator, Nat. Mater. 15, 542 (2016).
- [28] L. Zhang, Y. Yang, M. He, H. Wang, Z. Yang, E. Li, F. Gao, B. Zhang, R. Singh, J. Jiang, and H. Chen, Valley kink states and topological channel intersections in substrate-integrated photonic circuitry, Laser Photon. Rev. 13, 1900159 (2019).
- [29] B. Z. Xia, T. T. Liu, G. L. Huang, H. Q. Dai, J. R. Jiao, X. G. Zang, D. J. Yu, S. J. Zheng, and J. Liu, Topological phononic insulator with robust pseudospin-dependent transport, Phys. Rev. B 96, 94106 (2017).
- [30] X. Wu, Y. Meng, J. Tian, Y. Huang, H. Xiang, D. Han, and W. Wen, Direct observation of valley-polarized topological edge states in designer surface plasmon crystals, Nat. Commun. 8, 1304 (2017).
- [31] O. Isik and K. P. Esselle, Analysis of spiral metamaterials by Use of group theory, Metamaterials 3, 33 (2009).
- [32] Y. Long, J. Ren, and H. Chen, Intrinsic spin of elastic waves, Proc. Natl. Acad. Sci. U. S. A. 115, 9951 (2018).